NANO LETTERS

pubs.acs.org/NanoLett

Low-Frequency Acoustic Phonon Temperature Distribution in Electrically Biased Graphene

Insun Jo,[†] I-Kai Hsu,[‡] Yong J. Lee,[§,#] Mir Mohammad Sadeghi,[§] Seyoung Kim,[∥] Stephen Cronin,[⊥] Emanuel Tutuc,[∥] Sanjay K. Banerjee,[∥] Zhen Yao,[†] and Li Shi*[,§]

[†]Department of Physics, The University of Texas at Austin, Austin, Texas 78712, United States, [‡]Department of Materials Science and Engineering, University of Southern California, Los Angeles, California 90089, United States, [§]Department of Mechanical Engineering, The University of Texas at Austin, Austin, Texas 78712, United States, [∥]Department of Electrical and Computer Engineering, The University of Texas at Austin, Austin, Texas 78712, United States, [⊥]Department of Electrical Engineering, University of Southern California, Los Angeles, California 90089, United States, and [#]School of Mechanical Engineering, Kyungpook National University, 1370 Sankyuk-dong, Buk-gu, Daegu, 702-701, Korea

ABSTRACT On the basis of scanning thermal microscopy (SThM) measurements in contact and lift modes, the low-frequency acoustic phonon temperature in electrically biased, 6.7−9.7 μm long graphene channels is found to be in equilibrium with the anharmonic scattering temperature determined from the Raman 2D peak position. With ∼100 nm scale spatial resolution, the SThM reveals the shifting of local hot spots corresponding to low-carrier concentration regions with the bias and gate voltages in these much shorter samples than those exhibiting similar behaviors in the infrared emission maps.

KEYWORDS Graphene, electrical heating, scanning thermal microscopy, acoustic phonons, Raman spectroscopy

Single-layer graphene is considered a promising candidate for future-generation electronic devices because of the superior mobility of Dirac fermions in graphene.[1,2] The capability of the monatomic sheet of carbon atoms to carry an exceptionally large current density makes it attractive for realizing high-power electronic devices. As in state-of-the-art silicon nanoelectronic devices where the power density has increased drastically with decreasing feature size, heat dissipation and thermal management in high-power graphene devices have also become an important topic.

Several recent papers have reported the temperature measurements of some of the different energy carriers in electrically biased graphene devices at high current densities.[3−7] For example, thermal emission spectroscopy in the near-infrared[3,6] and visible range[4] has been measured and fitted with the Planck distribution to determine the electronic temperature, which reaches as high as 1570 K at a power density of 500 kW/cm^2. The ratio of anti-Stokes and Stokes Raman G mode has been used to deduce the temperature of the zone-center optical G phonons.[5] This method is accurate only when the temperature of the zone-center optical phonons is higher than about 600 K, below which the anti-Stokes peak is too small to be measured accurately. Nevertheless, the temperature of the optical G phonons has been found to be close to the electronic temperature, suggesting strong coupling between high-energy electrons and optical G phonons. Another method based on the Raman G band relies on the downward shift of the G band with increasing temperature.[8] The temperature determined from this method reflects the equivalent temperature of the anharmonic scattering processes between the zone-center optical phonons and the intermediate frequency phonons (IFPs),[9,10] although the position of the G peak is also known to be sensitive to impurity doping and strain.[9,11] Similarly, the shift of the Raman 2D band, involving the scattering of two zone-boundary optical phonons into IFPs, has been employed to estimate the equivalent temperature of these anharmonic decaying processes.[6,7] The work by Chae et al.[5] and Berciaud et al.[4] suggested that the IFPs may not be in full equilibrium with high-energy electrons and optical phonons, while the work by Freitag et al.[6] suggested that both the electrons and phonons were in full equilibrium.

Although these optical noncontact measurements have yielded a rich set of data of electronic and zone-center optical phonon temperatures, as well as the anharmonic scattering temperatures of zone-center and zone-boundary optical phonons, there is still a lack of direct measurement of the low-frequency acoustic phonon temperature. Without a direct measurement of the low-frequency acoustic phonon temperature, there would be insufficient data to verify whether various energy carriers are all in local equilibrium with the lattice. Moreover, low-frequency acoustic phonons

* Corresponding author. E-mail: lishi@mail.utexas.edu.
Received for review: 08/12/2010
Published on Web: 12/02/2010

DOI: 10.1021/nl102858c | *Nano Lett.* **2011,** *11,* 85–90

play an important role for heat dissipation, as they are primarily responsible for the in-plane thermal conductivity due to their large group velocity as well as the interfacial thermal conductance because of an increasing interface transmission coefficient with decreasing frequency at a van der Waals interface.[12,13] As such, they are relevant to the burn-out behavior of graphene. In addition, a disadvantage of the optical mapping methods is the spatial resolution that is limited by far field diffraction to be comparable to the wavelength. For example, IR emission spectroscopy has identified bias-dependent hot spot locations in electrically heated graphene devices.[3,6] So far, this observation has been limited to long-channel devices with a channel length longer than 25 μm. It is unclear whether the hot spots still exist in short-channel devices due to increased lateral heat transfer to the contacts.

In this letter, we report a contact measurement method for high-spatial resolution quantitative mapping of the low-frequency acoustic phonon temperature distribution in electrically biased graphene. With the use of a combined contact mode and lift mode operation of a scanning thermal microscopy (SThM) probe tip, we were able to determine the low-frequency acoustic phonon temperature profiles in the graphene channel with a spatial resolution on the order of 100 nm. Using this method, we were able to resolve bias-dependent hot spots in electrically biased graphene channels that were considerably smaller than those used in the IR mapping experiments.[3,6] In addition, the high-temperature sensitivity of the SThM technique allows us to examine the thermal behavior of the graphene in the low-power density regime that was not accessible by the optical techniques due to their limited temperature sensitivity. The measured acoustic phonon temperature was found to be close to the anharmonic scattering temperature determined from the Raman 2D-peak shift on the same sample.

The SThM sensor is a custom-made atomic force microscopy (AFM) tip with a submicrometer Pt−Cr thermocouple fabricated at the tip apex,[14,15] as shown in Figure 1a,b. When the thermocouple sensor is in contact with the sample, a thin oxide layer on the Cr surface prevents direct electronic coupling between the sensor and sample. On the other hand, phonon coupling across the tip−sample interface via the solid−solid contact and the surrounding liquid meniscus causes a change in the thermocouple temperature. With the low contact force used in the measurement, the phonon transmission coefficient across the weakly interacting interface is inversely proportional to ω^2, where ω is the phonon frequency.[12,13] Consequently, low-ω acoustic phonons in graphene make much larger contribution to the sensor temperature change than the high-ω phonons. For measurements in the ambient condition, parasitic heat transfer also occurs through the air gap between the sample and the cantilever. In this work, this contribution is eliminated by subtracting the thermovoltage obtained in the contact mode from that in the lift mode, based on the same principle demonstrated in a recent work.[16]

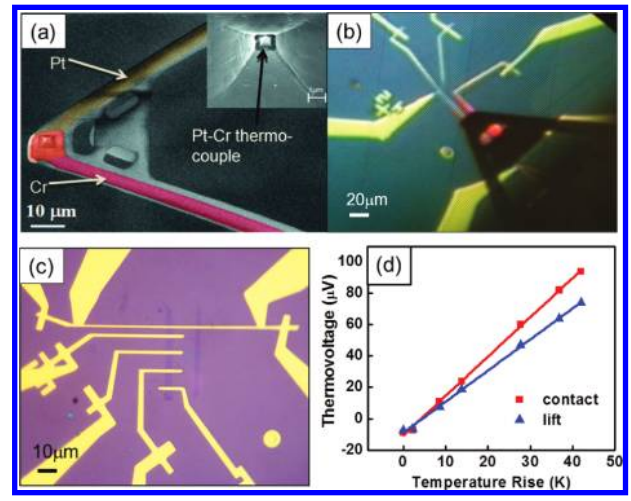

FIGURE 1. (a) Scanning electron micrograph (SEM) of the SThM probe with a submicrometer thermocouple fabricated at the apex of the tip. The inset shows the Pt−Cr thermocouple with a scale bar of 1 μm. (b) Optical micrograph of the SThM probe scanning over a graphene device. (c) Optical micrograph of a graphene device with four Au/Cr metal electrodes and an adjacent 100 μm long, 1 μm-wide Au/Cr heater and resistance thermometer line patterned on top of the graphene. (d) Thermovoltage signals of the SThM probe obtained at the center of the heater/thermometer line in the contact mode and lift mode with a 400 nm lift height as a function of the measured temperature rise of the heater/thermometer line.

Our devices were prepared using single-layer graphene exfoliated from natural graphite onto 300 nm thick SiO_2 thermally grown on a Si wafer. The single layer thickness was determined based on the color contrast in the optical microscope, and further verified using Raman spectroscopy. Electrodes consisting of a 5 nm thick chromium adhesion layer and 50 nm gold were deposited on the sample using electron beam lithography and metal lift off. Oxygen plasma patterning was used to define the rectangle-shaped graphene channel in the last step. Figure 1c shows the optical micrograph of a device consisting of patterned graphene connected to four electrodes as well as a 100 μm long Au/Cr heater and resistance thermometer line, which is used for temperature calibration, as discussed below. The results from three devices are presented in this paper. The channel length and width of the three devices are 6.7 μm × 3.8 μm (Device 1), 9.6 μm × 3.3 μm (Device 2), and 7.0. μm × 4.0 μm (Device 3), respectively. Figure 2a displays the linear-response resistance (R) as a function of silicon back gate voltage (V_{GS}) in Device 1, showing typical ambipolar behavior. The maximum resistance occurs at 4.5 V, corresponding to the Dirac point, $V_{GS\text{-}0}$. The dominant charge carriers to the left and right of $V_{GS\text{-}0}$ are holes and electrons, respectively. The carrier mobilities extracted from the R versus V_{GS} curves range from 6000 to 10 000 cm^2/(V s),[17] which is indicative of the high quality of our devices.

Figure 2b−d shows the contact-mode SThM measurements of Device 1 at different gate voltages and at a constant

DOI: 10.1021/nl102858c | *Nano Lett.* **2011,** *11,* 85–90

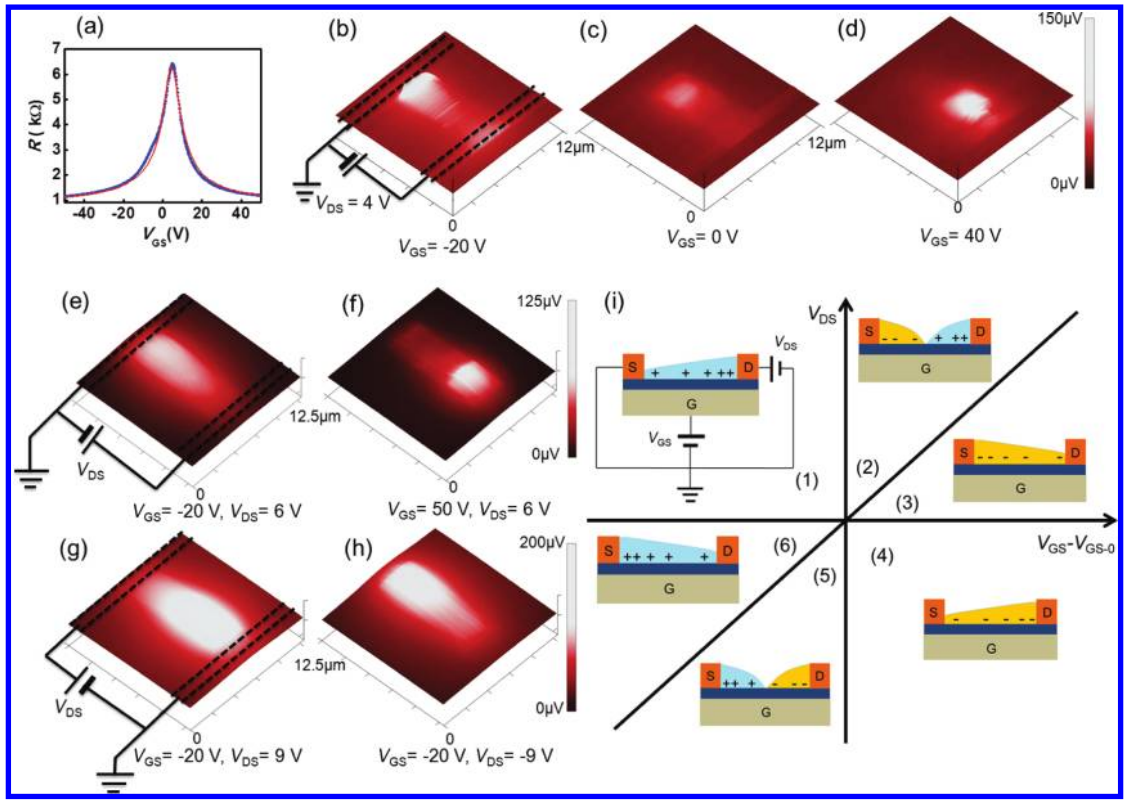

FIGURE 2. Thermal mapping of Device 1 and Device 2. (a) Two-probe low-bias resistance (blue line) of Device 1 as a function of the back gate voltage. The red line is the model fitting from which the mobility is extracted. (b−d) SThM thermovoltage maps of Device 1 for a constant drain-source bias (V_{DS} = 4 V) and different gate voltages of −20, 0, and 40 V, respectively. The scan size is 12 μm × 12 μm. (e−h) SThM thermovotlage maps of Device 2 for different combinations of bias and gate voltages. The electrode connections for f and h are the same as those shown for e and g, respectively. (i) Schematic illustration of the spatial distribution of the local charge carrier concentration in the graphene channel for different bias and gate voltages. Majority carriers can be either holes (blue +) or electrons (orange −). The source (S) electrode is grounded, and the V_{DS} is applied to the drain (D) electrode.

drain-source bias (V_{DS}) of 4 V. Remarkably, the thermovoltage signal exhibits a nonuniform profile along the graphene channel. For V_{GS} = −20 V, which makes the graphene channel hole doped, the temperature rise near the grounded source electrode is much higher than the other areas along the channel (Figure 2b). When V_{GS} was at 0 V and close to the Dirac point, the hot spot was found to have moved toward the middle of the channel (Figure 2c). When the gate bias was increased further to 40 V causing electron doping, the hot spot appeared on the drain electrode side (Figure 2d).

The obtained thermovoltage maps also display a strong dependence on the drain-source voltage. Figure 2e−h shows the thermovoltage maps measured on Device 2 under different bias conditions. The Dirac point for this device is ∼22 V. Similar to Device 1, at a positive drain-source voltage of 6 V, the hot spot shifted from the grounded source side on the left to the drain side on the right when the gate voltage was switched from negative to positive (Figure 2e,f). Upon exchanging the two contacts such that the right contact was grounded and a positive voltage was applied to the left contact, the hot spot again appeared near the grounded side as shown in Figure 2g. In the same hole-doped regime, when a negative voltage was applied to the drain, the hot spot shifted to the drain side, as shown in Figure 2h.

The origin of the hot spot has been discussed quantitatively in recent reports of infrared emission measurement results,[3,6] and is explained here by using a series resistance model in the graphene channel. The current density is homogeneous in our two terminal devices with a constant channel width. Hence, the local heating rate is proportional to the local resistivity, with the region of high temperature rise corresponding to the location of high resistivity, which is inversely proportional to the local carrier concentration assuming constant carrier mobility. The local carrier density is controlled by the effective electric potential $V_{eff}(x) = V_{GS} - V_{GS-0} - V(x)$, where $V(x)$ is the local electrochemical potential along the channel. This leads to different regimes of transport depending on the bias and gate voltages as shown in Figure 2i. For positive V_{DS} and negative $V_{GS} - V_{GS-0}$, the device is in the unipolar hole-doped regime (Regime 1 in Figure 2i). The hot spot thus occurs near the grounded source electrode where the hole density is the lowest (Figure 2b,e,g). For positive $V_{GS} - V_{GS-0}$ and small positive V_{DS} ($< V_{GS} - V_{GS-0}$), the device is in the unipolar electron-doped regime (Regime 3). Therefore, the hot spot appears near the drain contact where the electron density is the lowest (Figure 2d,f). For negative $V_{GS} - V_{GS-0}$, when V_{DS} is switched from positive to negative, the device remains in the hole-doped regime. However, the minimum in the hole density moves

DOI: 10.1021/nl102858c | *Nano Lett.* **2011,** *11,* 85–90

from the source to the drain (Regime 6). Hence the hot spot shifts from the source side to the drain side (Figure 2h). The profile shown in Figure 2c was obtained at zero gate voltage and positive V_{DS}, which should correspond to the hole-doped regime, similar to Figure 2b. However, the hot spot shows up in the middle of the channel. Since this image was acquired after $V_{GS} = -20$ V had been applied for a long time (~40 min) to obtain the image in Figure 2b, it is likely that the Dirac point had shifted to slightly negative value due to bias stress effect (see the Supporting Information). As a result, the device is now in the ambipolar regime (Regime 2), where the hot spot develops at the Dirac point inside the channel.

In order to quantify the acoustic phonon temperature in the graphene, we used a 100 μm long metal line heater and resistance thermometer patterned on the graphene to calibrate the SThM measurement results. The temperature coefficient of the metal line resistance was measured in a variable-temperature stage with a low excitation current. Subsequently, a dc heating current was flown between two wide metal electrodes to the thermometer line (Figure 1c). The resistance of the metal line was measured in a four-probe configuration and used to determine the average temperature rise in the metal line at different heating current levels. The temperature rise was measured to be 42 and 28 K at 18.56 mW and 12.15 mW electrical power dissipations in the heater line, respectively. Since the thermal contact resistance between the tip and the metal line and between the tip and graphene may be different, the calibration performed on the metal line cannot be directly applied to graphene. To resolve this issue, a finite element method (FEM) simulation was used to obtain the temperature distribution on the metal line as well as the graphene surface. In the model, the thermal conductivity of the heater line is obtained using the Wiedemann–Franz law based on the measured electrical resistivity of the heater line. The thermal conductivity values of SiO_2 and the supported graphene are taken to be 1.3 W/m·K and 600 W/m·K,[13,18] respectively. The calculated average temperature of the metal line is made to match the measurement results using the resistance thermometry method by adjusting the interface resistance between the metal line and the SiO_2 surface, which is found to be 1.0×10^{-8} m^{2}K/W. The value is consistent with the literature values for the metal–dielectric interface resistance and an order of magnitude larger than the interface resistance between SiO_2 and Si substrate.[19−21] We used the interface resistance value of 2.0×10^{-8} m^{2}K/W found at the Al–graphite interface for the metal–graphene interface resistance,[22] and 1.0×10^{-8} m^{2}K/W for the interface resistance between the graphene and the SiO_2 film.[23] These two interface resistances affect the graphene temperature profile close to the metal line, and the temperature of the short metal line segment located on top of graphene, but has little effect on the average temperature of the long metal line.

In order to eliminate the contribution of air conduction to the thermovoltage signals, SThM measurements were conducted in both contact and lift modes on the sample heated using the metal line heater. Figure 1d shows such measurements obtained at the center of the metal heater line. The thermovoltage signal obtained in the lift mode is caused mostly by heat transfer through the air gap between the sample and the probe including both the tip and the cantilever, and is insensitive to the lift height when the lift height is much smaller than the ~8 μm height of the tip (see the Supporting Information).[14] In our measurements, the thermovoltage signal obtained in lift mode at a lift height of 400 nm was subtracted from that obtained in the contact mode. The resultant signal is caused by heat transfer due to low-frequency acoustic phonons through the solid–solid contact and the surrounding liquid meniscus. The ratio of the obtained thermovoltage difference between the two SThM modes over the calculated sample surface temperature is 0.53 μV/K and 0.63 ± 0.04 μV/K when the tip was on the metal line and graphene, respectively.

With the same contact pressure and lift height as those used in the calibration, the hybrid contact-lift mode SThM measurements were conducted on Device 3 (Figure 3). From low-bias R versus V_{GS} measurement, the Dirac point of this sample is located at $V_{GS\text{-}0} = 16$ V. The SThM measurements were conducted at $V_{GS} = 0$ V to prevent any spurious doping due to the gate bias.[3,24,25] At $V_{GS} = 0$ V, the corresponding Fermi level is determined to be −0.135 eV, so that the majority carriers are holes at a positive V_{DS}. Similar to the other samples, the position of the hot spot was found to correspond to the region of low local carrier density. On the basis of the obtained temperature response ratio of the SThM tip on graphene, the temperature rise in the channel was determined from the difference between the two measured thermovoltage values obtained in the contact and the lift modes. The maximum temperature rise of the low-frequency acoustic phonons in the graphene was found to be 160 K at $V_{DS} = -6.5$ V, as shown in Figure 3c. The average temperature rise of the graphene channel increases linearly with the power density (Figure 3e), calculated as the electrical power divided by the area of the graphene channel. A linear fit to the data yields an equivalent thermal resistance of 7735 K/W for the sample. This resistance value is in good agreement with the sum of the 7653 K/W thermal resistance of the underlying 300 nm thick oxide spacer of the same dimension as the graphene, a graphene–SiO_2 interface resistance of 357 K/W,[23] and a 608 K/W spreading resistance of the Si substrate.[26,28] In comparison, the thermal resistance for lateral heat spreading along the graphene is on the order of 4×10^6 K/W, which is much larger than the thermal resistance for heat conduction into the substrate.[28] This comparison suggests that vertical heat dissipation to the SiO_2 support dominates over lateral heat dissipation to the metal electrode even for these graphene samples that are considerably shorter than those used in the IR measurements,[3,6] similar to the situation of electrically biased single-walled carbon nanotubes.[15]

After the SThM measurements were completed, we conducted Raman spectroscopy measurements of Device 3 to determine the temperature from the Raman 2D and G

DOI: 10.1021/nl102858c | Nano Lett. 2011, 11, 85–90

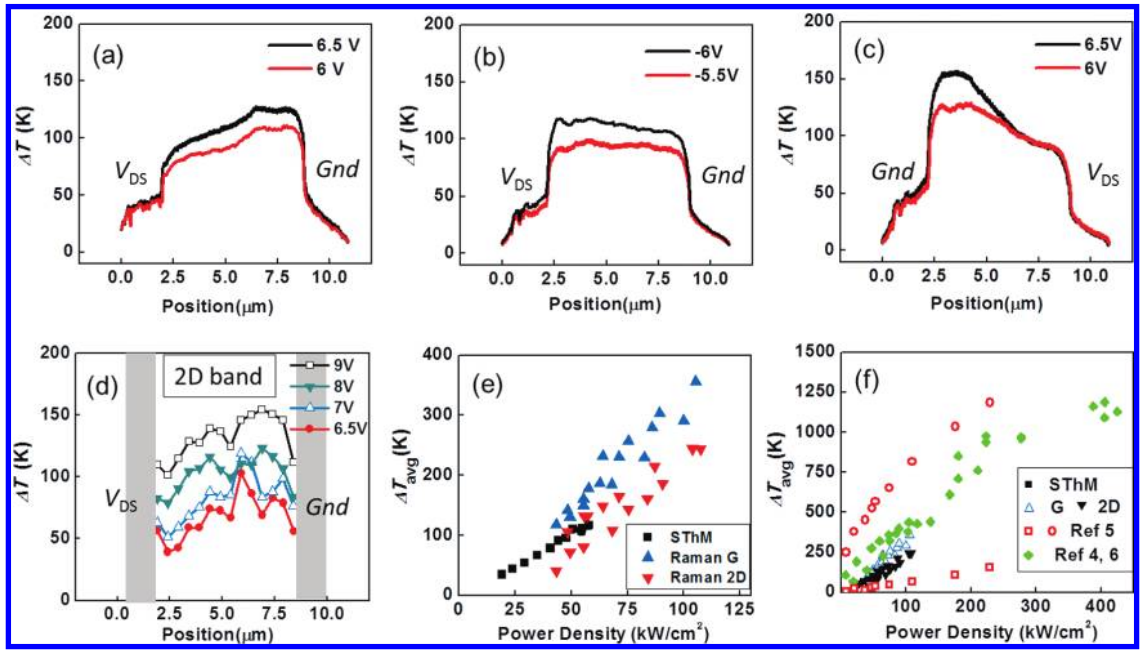

FIGURE 3. Comparison of temperatures determined from SThM measurement and Raman measurement. (a−c) Measured SThM temperature profiles in Device 3 at different V_{DS} values and polarities and $V_{GS} = 0$ V. (d) Raman 2D band temperature profile measured on the same device at different V_{DS} values and $V_{GS} = 0$ V. *Gnd* refers to the ground electrode. The shaded areas indicate the locations of the two electrodes. (e) Average temperature rise in the graphene channel measured by the SThM as well as Raman G and 2D peak shifts as a function of power density. (f) Average temperature rise as a function of power density obtained using SThM (black squares), Raman G band shift (open upper triangles), and 2D band shift (down triangles) from the present work and previous optical measurement results including the Raman G band temperature in ref 5 (red open squares), the temperature determined from the anti-Stokes/Stokes ratio in ref 5 (red open circles), and the temperatures measured by using IR emission, Raman 2D and G band shifts, and the anti-Stokes/Stokes ratio in refs 4 and 6 (green diamonds).

peak shifts at various power densities. The Raman D peak associated with defects was absent,[27] suggesting that the small contact force during the SThM measurement did not cause damage to the graphene (see the Supporting Information). When the graphene was heated by an external sample stage, the Raman 2D and G peaks shift with temperature at a rate of -0.057 cm^{-1}/K and -0.022 cm^{-1}/K, respectively. These values were used to convert the measured 2D and G peak shifts to temperatures during self-electrical heating of the graphene sample. The obtained 2D and G band temperature profiles in the graphene channel showed asymmetric heating (see the Supporting Information). The 2D profile shown in Figure 3d is qualitatively similar to the SThM results, although the Raman profile does not reproduce the fine features in the SThM profile (Figure 3a). The average temperatures extracted from the 2D and G measurements along the graphene channel are plotted together with the SThM results as a function of the power density in Figure 3e. The Raman 2D temperature shows reasonably good agreement with the linear fitting of the low-frequency acoustic phonon temperatures measured by the SThM in the low-power density region. On the other hand, the G peak temperature appears to be slightly higher than both the 2D temperatures and the SThM temperatures, presumably caused by the influence of impurity doping and strain.[7,9,11]

Because both of our SThM and Raman measurements were conducted in air, the power density could not be increased to a sufficiently high level for the anti-Stoke signal to be observed without sample burn-out.[5] In Figure 3f, we have plotted our temperature versus power density results together with literature data obtained using the Raman and thermal emission measurements performed in vacuum and mostly at higher power density.[4−6] Except for the 1.5 μm × 0.6 μm graphene constriction sample reported in ref 5, all the data appear to converge onto a single curve, suggesting that the temperatures of different energy carriers measured by different methods are approximately in equilibrium with each other in these relatively large-area graphene samples. Moreover, the temperatures appear to follow a linear dependence on the power density. Because the slope of the curve is equivalent to the thermal resistance per unit area, this convergence suggests that the thermal resistance in these devices is mainly determined by the underlying SiO_2 spacer due to dominant vertical heat transport. For the graphene constriction sample, the zone-center optical phonon temperature measured by the anti-Stokes to Stokes ratio is considerably higher, and the anharmonic temperature of the G band shift is considerably lower than the fitting to the other data. Besides impurity doping and strain, the lower anharmonic G band temperature in the constriction sample could be caused by the increasing importance of lateral heat conduction by acoustic phonons from the graphene to the metal electrodes, as well as a relatively small spreading thermal resistance component of the Si substrate that scales inversely with the lateral dimension instead of area

DOI: 10.1021/nl102858c | *Nano Lett.* **2011,** *11,* 85–90

as for the thermal resistance of the SiO_2 spacer.[28] The presence of hot optical phonons in the constriction also suggests strong coupling between the hot electrons and zone-center optical phonons compared to surface polar optical phonon scattering and coupling of optical phonons with lower-energy phonons. The clear observation of hot optical phonons only in the constriction sample deserves further investigation.

In summary, our high-spatial resolution SThM measurement results suggest that asymmetric heating due to inhomogeneous charge carrier concentration also occurs in several micrometer-long graphene channels that are considerably shorter than those observed using IR mapping. By subtracting the signal measured in the lift mode due to parasitic air conduction from that measured in the contact mode, we have obtained the temperature distribution of the low-frequency acoustic phonons in graphene that dominate the heat transfer through the van der Waals contact and the surrounding liquid meniscus. The obtained average temperature of the low-frequency acoustic phonons increases linearly with the power density and is in equilibrium with the anharmonic scattering temperature of Raman 2D phonons measured on the same sample. The slope of the average temperature rise versus power density curve obtained by SThM at low power density is consistent with those measured using optical techniques in graphene channels of similar or larger sizes at higher power density. This comparison suggests that the different energy carriers in graphene channels larger than several micrometers in size are in equilibrium, with their average temperature rise close to the power density divided by the thermal resistance per unit area of the underlying SiO_2 layer.

Acknowledgment. This work was supported in part by Department of Energy Awards DE-FG02-07ER46377 and DE-FG02-07ER46376, the National Science Foundation Thermal Transport Processes Program, and the Texas Higher Education Coordinating Board Norman Hackerman Advanced Research Program.

Supporting Information Available. Details of device fabrication and characterization, experimental data showing bias stress effect, thermovoltage measurements with the contact and the lift mode in SThM, derivation of the temperature calibration method, details of FEM simulation used for the calibration, and the temperature profiles obtained using Raman 2D and G band shifts. This material is available free of charge via the Internet at http://pubs.acs.org.

REFERENCES AND NOTES

(1) Geim, A. K.; Novoselov, K. S. *Nat. Mater.* **2007**, *6*, 183–191.
(2) Lin, Y. M.; Jenkins, K. A.; Valdes-Garcia, A.; Small, J. P.; Farmer, D. B.; Avouris, P. *Nano Lett.* **2009**, *9*, 422–426.
(3) Bae, M. H.; Ong, Z. Y.; Estrada, D.; Pop, E. *Nano Lett.* **2010**, DOI: 10.1021/nl1011596.
(4) Berciaud, S.; Han, M. Y.; Mak, K. F.; Brus, L. E.; Kim, P.; Heinz, T. F. *Phys. Rev. Lett.* **2010**, *104*, 227401.
(5) Chae, D. H.; Krauss, B.; von Klitzing, K.; Smet, J. H. *Nano Lett* **2010**, *10*, 466–471.
(6) Freitag, M.; Chiu, H. Y.; Steiner, M.; Perebeinos, V.; Avouris, P. *Nat. Nanotechnol.* **2010**, *5*, 497–501.
(7) Freitag, M.; Steiner, M.; Martin, Y.; Perebeinos, V.; Chen, Z. H.; Tsang, J. C.; Avouris, P. *Nano Lett.* **2009**, *9*, 1883–1888.
(8) Calizo, I.; Miao, F.; Bao, W.; Lau, C. N.; Balandin, A. A. *Appl. Phys. Lett.* **2007**, *91*, No. 071913.
(9) Basko, D. M.; Piscanec, S.; Ferrari, A. C. *Phys. Rev. B* **2009**, *80*, 165413.
(10) Bonini, N.; Lazzeri, M.; Marzari, N.; Mauri, F. *Phys. Rev. Lett.* **2007**, *99*, 176802.
(11) Das, A.; Pisana, S.; Chakraborty, B.; Piscanec, S.; Saha, S. K.; Waghmare, U. V.; Novoselov, K. S.; Krishnamurthy, H. R.; Geim, A. K.; Ferrari, A. C.; Sood, A. K. *Nat. Nanotechnol.* **2008**, *3*, 210–215.
(12) Prasher, R. *Appl. Phys. Lett.* **2009**, *94*, No. 041905.
(13) Seol, J. H.; Jo, I.; Moore, A. L.; Lindsay, L.; Aitken, Z. H.; Pettes, M. T.; Li, X. S.; Yao, Z.; Huang, R.; Broido, D.; Mingo, N.; Ruoff, R. S.; Shi, L. *Science* **2010**, *328*, 213–216.
(14) Shi, L.; Majumdar, A. *J. Heat Transfer - Trans. ASME* **2002**, *124*, 329–337.
(15) Shi, L.; Zhou, J. H.; Kim, P.; Bachtold, A.; Majumdar, A.; McEuen, P. L. *J. Appl. Phys.* **2009**, *105*, 104306.
(16) Kim, K.; Chung, J.; Won, J.; Kwon, O.; Lee, J. S.; Park, S. H.; Choi, Y. K. *Appl. Phys. Lett.* **2008**, *93*, 203115.
(17) Kim, S.; Nah, J.; Jo, I.; Shahrjerdi, D.; Colombo, L.; Yao, Z.; Tutuc, E.; Banerjee, S. K. *Appl. Phys. Lett.* **2009**, *94*, No. 062107.
(18) Cahill, D. G.; Bullen, A.; Lee, S. M. *High Temp. - High Pressures* **2000**, *32*, 135–142.
(19) Kading, O. W.; Skurk, H.; Goodson, K. E. *Appl. Phys. Lett.* **1994**, *65*, 1629–1631.
(20) Kim, J. H.; Feldman, A.; Novotny, D. *J. Appl. Phys.* **1999**, *86*, 3959–3963.
(21) Yamane, T.; Nagai, N.; Katayama, S.; Todoki, M. *J. Appl. Phys.* **2002**, *91*, 9772–9776.
(22) Schmidt, A. J.; Chen, X. Y.; Chen, G. *Rev. Sci. Instrum.* **2008**, *79*, 114902.
(23) Chen, Z.; Jang, W.; Bao, W.; Lau, C. N.; Dames, C. *Appl. Phys. Lett.* **2009**, *95*, 161910.
(24) Lafkioti, M.; Krauss, B.; Lohmann, T.; Zschieschang, U.; Klauk, H.; von Klitzing, K.; Smet, J. H. *Nano Lett.* **2010**, *10*, 1149–1153.
(25) Zilker, S. J.; Detcheverry, C.; Cantatore, E.; de Leeuw, D. M. *Appl. Phys. Lett.* **2001**, *79*, 1124–1126.
(26) Asheghi, M.; Kurabayashi, K.; Kasnavi, R.; Goodson, K. E. *J. Appl. Phys.* **2002**, *91*, 5079–5088.
(27) Ferrari, A. C.; Meyer, J. C.; Scardaci, V.; Casiraghi, C.; Lazzeri, M.; Mauri, F.; Piscanec, S.; Jiang, D.; Novoselov, K. S.; Roth, S.; Geim, A. K. *Phys. Rev. Lett.* **2006**, *97*, 187401.
(28) The thermal resistance of the SiO_2 spacer between the graphene and the Si substrate is estimated as $R_{SiO2} \approx t_{SiO2}/(\kappa_{SiO2}WL)$, where $t_{SiO2} = 300$ nm and κ_{SiO2} are the thickness and the thermal conductivity of the SiO_2 film, respectively, and W and L are the width and length of the graphene channel, respectively. The spreading thermal resistance of the Si substrate is calculated using the conduction shape factor as $R_{Si} \approx 1/(2\kappa_{Si}(WL)^{1/2})$,[29] where κ_{Si} is the thermal conductivity of the silicon substrate. The thermal resistance for lateral heat spreading from the graphene to the metal electrodes is on the order of $R_g \approx L/(2\kappa_g Wt)$, where κ_g and t are the thermal conductivity and thickness of the supported graphene, respectively. Compared to R_g, the thermal resistance of the relatively thick metal electrodes of high thermal conductivity is negligible, as verified by the negligible heating measured on top of the metal electrodes by SThM.
(29) Incropera, F. P.; Dewitt, D. P.; Bergman, T. L.; Lavine, A. S. *Fundamentals of Heat and Mass Transfer*; John Wiley & Sons: New York, 2007; pp 210.

DOI: 10.1021/nl102858c | *Nano Lett.* **2011,** *11,* 85–90